Quantitative analysis of shadow X-ray Magnetic Circular Dichroism Photo-Emission Electron Microscopy

Ségolène Jamet, Sandrine da Col, Nicolas Rougemaille, Alexis Wartelle, Andrea Locatelli, T.O. Mentes, B. Santos Burgos, Raja Afid, Laurent Cagnon, Julien Bachmann, et al.

Quantitative analysis of shadow X-ray Magnetic Circular Dichroism Photo-Emission Electron Microscopy

S. Jamet,[1,2] S. Da Col,[1,2] N. Rougemaille,[1,2] A. Wartelle,[1,2] A. Locatelli,[3] T. O. Menteş,[3] B. Santos Burgos,[3] R. Afid,[1,2] L. Cagnon,[1,2] J. Bachmann,[4] S. Bochmann,[4] O. Fruchart,[1,2] and J. C. Toussaint[1,2]

[1] *Universtité Grenoble Alpes, Inst NÉEL – F-38042 Grenoble – France*
[2] *CNRS, Inst NÉEL, CNRS – F-38042 Grenoble – France*
[3] *Elettra - Sincrotrone Trieste S.C.p.A., I-34012 Basovizza, Trieste, Italy*
[4] *Department of Chemistry, Univ. Erlangen, Erlangen, Germany*

(Dated: June 18, 2015)

Shadow X-ray Magnetic Circular Dichroism Photo-Emission Electron Microscopy (XMCD-PEEM) is a recent technique, in which the photon intensity in the shadow of an object lying on a surface, may be used to gather information about the three-dimensional magnetization texture inside the object. Our purpose here is to lay the basis of a quantitative analysis of this technique. We first discuss the principle and implementation of a method to simulate the contrast expected from an arbitrary micromagnetic state. Text book examples and successful comparison with experiments are then given. Instrumental settings are finally discussed, having an impact on the contrast and spatial resolution : photon energy, microscope extraction voltage and plane of focus, microscope background level, electric-field related distortion of three-dimensional objects, Fresnel diffraction or photon scattering.

Progress is continuous in the decreasing size and increasing complexity of nanosized magnetic systems being designed for either fundamental science or devices. Magnetic microscopies are crucial tools to monitor and understand the properties of such systems. Various types of information are desirable to gather, leading to multiple criteria to classify microscopies: spatial and time resolution, compatibility with environmental parameters such as variable temperature and applied magnetic field, requirements on the sample preparation and compatibility for ex-situ processing such as lithography, correlation with structural information, elemental sensitivity, quantity measured (magnetization, induction, stray field etc.), sensitivity. The most common magnetic microscopic methods offering spatial resolution below 50 nm and direct sensitivity to magnetization are X-ray Magnetic Circular Dichroism Photo-Emission Electron Microscopy (XMCD-PEEM)[1] and (Scanning) Transmission X-ray Microscopy [(S)TXM][2], electron holography or Lorentz microscopy[3–5], Scanning Electron Microscope with Polarization Analysis (SEMPA)[6], Spin-Polarized Low-Energy Electron Microscopy (SPLEEM)[7, 8].

Yet another criterion is the volume of the sample probed. SPLEEM and SEMPA typically probe the topmost atomic layer of matter. This makes them sensitive to very small amounts of material if layered, however hides magnetic information in the core of a system. On the reverse, Lorentz, Holography and (S)TXM are transmission techniques with a penetration depth of the order of 100 nm, providing information about volume magnetic textures over this depth. However, these have a lower sensitivity, and average the measured signal along the path of the beam, thus loosing information in the case of magnetic textures varying along the depth. The probing depth of XMCD-PEEM is intermediate, being a few nanometers and related to the mean free path of the secondary electrons used for imaging. Thus it is not strictly surface sensitive, however not suitable a priori to probe magnetic systems in depth.

Recently XMCD-PEEM was applied to three-dimensional objects lying on a supporting surface[9–13]. As the X-ray beam is tilted with respect to the normal to the supporting surface, this provides magnetic sensitivity both at the surface of the object, and gives rise to a shadow on the supporting surface whose inspection yields information about magnetization in the core (Figure 1a). This has been named shadow XMCD-PEEM [9]. This provides a technique with an interesting hybrid sensitivity, within the set of microscopy techniques mentioned above. It shall be of use for the analysis of three-dimensional magnetic objects and textures, a topic of rising importance [9, 13–20]. However, due to the three-dimensional shape of the objects considered, and the depth- and helicity-dependent absorption of X-rays through the structure, the magnetic contrast cannot simply be interpreted as the projection of magnetization along the direction of the beam, as it is the case for the usual surface XMCD-PEEM. In Ref.[19] the authors simulated the contrast in the shadow of a rolled tube, however based on an analytical form for the distribution of magnetization in a thin sheet. Also, the contrast at the surface of the structure was not computed.

In this manuscript we will review specific aspects of shadow XMCD-PEEM, and propose a method to analyze the resulting images of surface and shadow based on the complete micromagnetic structure of an object, to make shadow XMCD-PEEM a quantitative technique. The manuscript is organized as follows. First the principles and implementation of a method to simulate the contrast of three-dimensional magnetization textures are described. Then we illustrate the simulations with two test cases. Comparison with a few experimental cases is then made, followed by a discussion of the constraints for

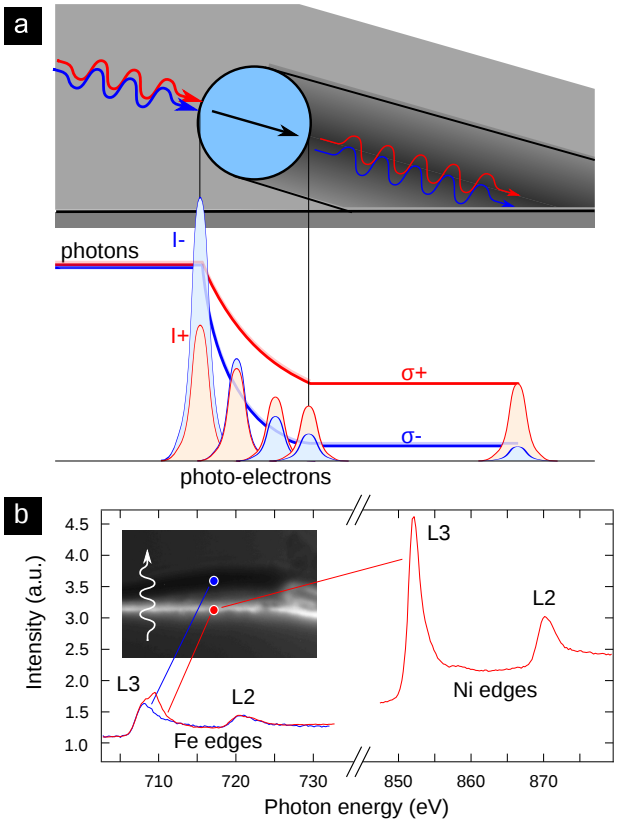

Figure 1: **XAS and XMCD of cylindrical wires.** (a) illustration of the the principle of the dual surface and volume contrast on the basis of the test case of magnetization parallel to the X-ray beam. The curves below represent the polarization-dependent X-ray intensity at the absorption peak as the X-rays propagate through the wire section. (b) Red: absorption spectra across the Fe and Ni L edges normalized to the background signal (absorption on the supporting Si surface). Blue: inverted and normalized spectra measured in the shadow. Note that the spectrum from the wire surface reflects oxidized Fe due to air exposure, whereas the shadow spectrum shows mostly metallic iron as it derives from the bulk of the wire.

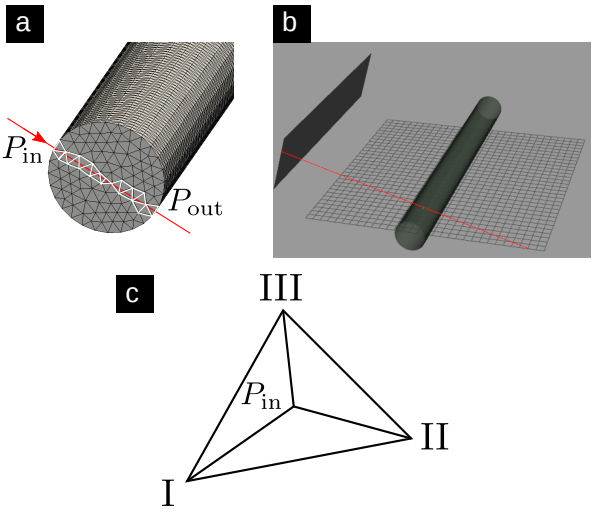

Figure 2: **Description of the numerical method.** The system considered is a cylindrical nanowire. (a) presents the method to model the X-ray beam. The red line presents the X-ray beam that crosses the elements (in white, from the finite element discretization). Surface elements of the discretized physical system are in grey green. (b) shows the wire on the gridded supporting surface and the photon source. (c) scheme of a surface triangle to illustrate the method of the areal coordinates.

Table I: Absorption coefficients μ at the different absorption edges. Figures for pure elements are derived from [21]

Edge	μ (nm^{-1})	Fe	Ni	$Fe_{20}Ni_{80}$
Fe L2	μ_-	0.03	≈ 0	0.006
	μ_+	0.04	≈ 0	0.008
Fe L3	μ_-	0.09	≈ 0	0.018
	μ_+	0.05	≈ 0	0.010
Ni L2	μ_-	0.017	0.017	0.017
	μ_+	0.017	0.021	0.020
Ni L3	μ_-	0.017	0.053	0.046
	μ_+	0.017	0.040	0.035

the quantitative analysis of magnetic contrast and spatial resolution. These are largely related to finer points of the physics at play, which have so far been left aside in the modeling.

I. METHOD AND IMPLEMENTATION OF THE SIMULATIONS

Our approach consists in considering a given three-dimensional magnetization texture in a system, and use it as an input to simulate the XAS and XMCD contrasts expected at both the surface and in the shadow. The magnetic texture may be a simple analytical form, or a realistic distribution of magnetization resulting from a micromagnetic simulation. In this section we first describe the physical principles considered to convert a magnetic texture into a magnetic contrast. Then we detail the practical implementation in the numerics.

A. Principle of the method

Building an XMCD-PEEM image requires to describe mainly three distinct steps including physical and instrumental aspects: 1. Absorption through matter 2. Photoemission of electrons close to surfaces 3. Collection of these electrons in the microscope. The way we model each of these processes is detailed below.

Let us first consider X-ray absorption. At any stage when traveling through matter, an X-ray beam is associated with a probability of absorption per unit length, μ, determining the mean free path of photons $\lambda = 1/\mu$.

These parameters depend on the composition of matter, as well as on the photon energy. We considered photons at the L_3 and L_2 edges of both Fe and Ni, and used the experimentally determined parameters from the literature [21] for pure elements and both helicities of photons. We assumed that the absorption coefficient of Permalloy is $\mu = 0.2\mu_{\mathrm{Fe}} + 0.8\mu_{\mathrm{Ni}}$. Absorption coefficients at the different edges are summarized in Table I. At the Fe L edges, absorption due to Fe is very large, and the pre-edge absorption of Ni is very weak, so that despite the low concentration of Fe it is by far the dominating contribution. At the Ni L edges the post-edge absorption of Fe is in principle no more negligible especially because absorption on Ni with a nearly filled $3d$ band yields less intensity. The contribution of Ni is however still larger, due to its mich larger concentration.

The progressive absorption of the beam in matter is obtained by integrating its position-sensitive rate of absorption through a thickness $\mathrm{d}\ell$ of material:

$$\frac{\mathrm{d}I_{X,\sigma\pm}}{\mathrm{d}\ell} = -\left[\frac{1}{2}\mu_+(1 \pm \hat{\mathbf{k}}\cdot\mathbf{m}) + \frac{1}{2}\mu_-(1 \mp \hat{\mathbf{k}}\cdot\mathbf{m})\right] I_{X,\sigma\pm} \tag{1}$$

where μ_+ and μ_- stand for the absorption coefficients for left and right circularly polarized X-rays, respectively. This formula takes into account the energy and helicity dependence, in relation with the direction of magnetization when in the sample, with $\hat{\mathbf{k}}$ the unit vector along the propagation direction.

In a second step we need to estimate the local rate of emission of secondary photoelectrons $I_{e,\sigma}(\mathbf{r}_\mathrm{s})$ at any location $\mathbf{r}_\mathrm{s}$ at the surface, resulting from the transmitted X-ray intensity reaching that location as calculated previously. In PEEM the escape depth of the secondary photoelectrons is only a few nanometers. As this length is much smaller than the diameter of the wires considered in the experiments, and also smaller than any magnetic length scale, we used the simplifying assumption that on the wire $I_{e,\sigma}(\mathbf{r}_\mathrm{s})$ reflects $I_{X,\sigma}(\mathbf{r}_\mathrm{s})$ and magnetization at the surface, through again dichroism. To the contrary, when impinging on the non-magnetic surface, for instance in the shadow, the photons give rise to a rate of electrons directly proportional to $I_{X,\sigma}(\mathbf{r}_\mathrm{s})$. For a quantitative analysis the rate of absorption and electron emission should be calibrated with the XAS on both the magnetic material and the supporting surface. Care should however been taken, as in practice this rate sensitively depends on the extraction voltage used for imaging [see sec.IV and Figure 7(d-f)]. Let us finally discuss the escape of electrons from matter. Theoretically photo-emitted electrons are emitted isotropically and not perpendicular to the local nor mean surface of the sample. Thus, we expect that a measured image results from convolution of the signal described right before, and a function describing this scattering processes, including production of secondary electrons. In practice however, as the depth of escape of electrons is only a few nanometers, the expected broadening should not exceed these few nanometers, which is much smaller than the instrumental resolution (circa 30nm). Thus, these effects may be safely neglected. At this stage we have an estimate $I_{e,\sigma}(\mathbf{r}_\mathrm{s})$ of the local emission of electrons at each point of the nanostructure and its supporting surface.

As a third step we now need to convert this into the intensity per unit surface $I_s(x, y)$, on the detector. One important parameter to make the link between $I_{e,\sigma}(\mathbf{r}_\mathrm{s})$ and $I_s(x, y)$ is the angular acceptance of the microscope. Indeed, secondary electrons are emitted on the average along the normal to the local surface, with an angle θ with respect to the axis of the imaging column as shown in Figure 3a [22]. The collected photoelectron signal is maximized for surfaces with the surface normal along the microscope optical axis. Signal from tilted surfaces are suppressed with increasing tilt angle at the so-called angle-selecting aperture. However the exact angular dependance is not well characterized and may depend sensitively on extraction and electron energy, aperture, surface roughness etc. Thus we did not attempt to consider a realistic transfer function, as this would be largely arbitrary. We simply projected $\mathbf{r}_\mathrm{s}$ onto the plane of the supporting surface to get (x, y) coordinates. This is equivalent to using a $\cos\theta$ collection function. While the collection function affects the XAS (SUM signal), theoretically XMCD images should not depend on this function as they are computed as differences normalized by the sum. In practice, due to the reduced number of photons in areas where the real transfer function does not allow the collection of electrons, combined with a background electron level to be discussed in sec.IV C, in experimental images the XMCD may be sharply decreased in such areas.

Let us note that the above procedure is not a bijection but a surjection, because of the integration along a path and also of the projection of magnetization along the beam. Thus, one XPEEM image may in principle correspond to different magnetic configurations. This, along with other issues contributing to image formation such as photon scattering, field distortion due to wire topography, and background electron intensity, will be discussed further below (sec.IV).

B. Numerical implementation

Besides analytic test cases, micromagnetic configurations resulting from simulations are used as input to compute the XMCD contrast. For the micromagnetic configurations, we use the home-made code FeeLLGood[23]. FeeLLGood is based on the finite element method. We used material parameters suitable for Permalloy: $A = 10\,\mathrm{pJ/m}$, $\mu_0 M_\mathrm{s} = 1\,\mathrm{T}$. The damping parameter α was set to 1 to facilitate convergence, with no impact on the results as we only consider states at rest. No magnetocristalline anisotropy was considered.

In the present study we consider cylindrical nanowires. The principle of the numerical method is to launch a ray, then to compute the absorption along this ray according

to the magnetization of the sample, and finally to save the photoelectron intensity. We first simulate the flux of photons $I_{X,\sigma}(\mathbf{r})$ with a given helicity at any position in space, inside and outside the magnetic system. For this we consider a regular planar grid perpendicular to the direction of the photons of an incident plane wave. From each node a ray is launched and intercepts the surface of the cylinder at two points P_{in} and P_{out} respectively called the entering and exit points. We estimate magnetization at these points using the following method (see Figure 2). At P_{in} and P_{out} the magnetization is interpolated from the nodal values of the triangle to which it belongs using a method based on the areal coordinates method [24]. This triangle with three nodes (I, II, III) is divided into sub-triangles with a common vertex P_{in}. Then the polynomials, used for the interpolation of the magnetization, are calculated such that the one associated to the node I is the ratio between the surface of the triangle (P_{in}, II, III) and the total surface of the triangle (Figure 2c). The same method is applied for the other two nodes. In order to calculate the absorption along the ray the latter is discretized into segments of a given length between P_{in} and P_{out}. The points that separate these segments are the place of the calculation of the corresponding magnetization. For each discretization point first we determine the corresponding element (tetrahedron in the volume of the wire, see Figure 2b). The magnetization is interpolated with the method previously described but with four nodes and making use of sub-tetrahedrons instead of sub-triangles. Once the local magnetization has been computed, the absorption along the entire path through the magnetic structure is computed. It is done by integrated equation 1: $I_{X,\sigma_\pm} \propto \exp\left\{-\int_{P_{\text{in}}}^{P_{\text{out}}} \mathrm{d}\ell \left[\frac{1}{2}\mu_+(1 \pm \hat{\mathbf{k}}\cdot\mathbf{m}) + \frac{1}{2}\mu_-(1 \mp \hat{\mathbf{k}}\cdot\mathbf{m})\right]\right\}$.

The next step is to get the intensity of the photoelectrons emitted after the absorption of X-rays. At the surface of the wire, the intensity of the photoelectrons is then calculated as the intensity of the photons multiplied by a pre-factor and normalized by the density of X-ray flux $\mathbf{n}\cdot\hat{\mathbf{k}}$. The pre-factor takes into account the scalar product of the local magnetization and the wave vector and the local absorption coefficient such that :

$$I_{e^-,\sigma_\pm} \propto \frac{1}{\mathbf{n}\cdot\hat{\mathbf{k}}}\frac{2}{\mu_+ + \mu_-}\left[\frac{1}{2}\mu_+(1 \pm \hat{\mathbf{k}}\cdot\mathbf{m}) + \frac{1}{2}\mu_-(1 \mp \hat{\mathbf{k}}\cdot\mathbf{m})\right] I_{X,\sigma_\pm}. \quad (2)$$

Note that the right hand side is the derivative of X-ray intensity along the propagation path (as in equation 1). The physical sense is much clearer, because the derivative of $I_{X,\sigma}$ is the amount of photons absorbed within that incremental distance, and the photoemission is directly proportional to the absorption.

The last step is to save the computed photoelectron intensity at each point of the wire surface to the detector grid. At P_{in} with coordinates (x, y, z), is associated

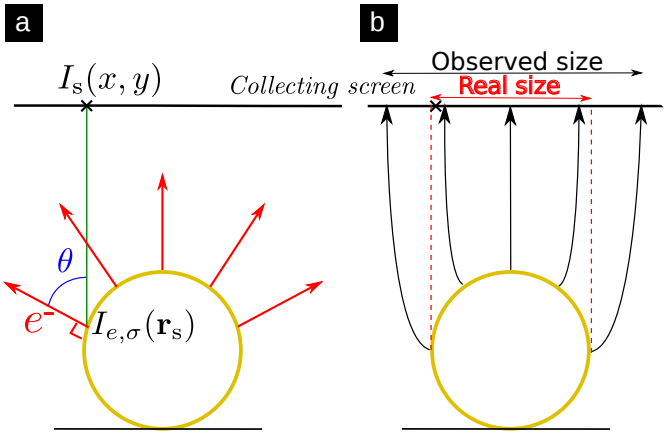

Figure 3: (a) illustration of the collection of the photoelectrons. $\mathbf{e}^-$ is the secondary electron emission direction. θ is the angle between the imaging axis and the latter direction. (b) Illustrates the distortion of the photoelectron trajectory (see sec.V).

$I_s(x, y)$ on the screen. These coordinates do not necessarily correspond to the center of a grid cell. Moreover the photoelectrons are no more equispaced after being emitted from the wire. To define the problem better we determine the corresponding detector cell of coordinates (x, y) and the nearest neighbours so as to smooth the contrast. The photoemission from a point P_{ext} on the substrate is proportional to the intensity of x-rays as they exit the magnetic structure at point P_{out}. The dichroism observed at the P_{ext} is due to the dichroism in the transmitted intensity through the structure. The secondary electrons are ejected normal to the surface. The intensity is saved on the detector in the same way. Finally all the XMCD-PEEM contrast is constructed by taking the difference $(I_{e,-} - I_{e,+})$ and normalizing it to the sum $(I_{e,-} + I_{e,+})$. The implementation has been done by using the geometry library CGAL [25] for the use of rays, and the nearest neighbourg searching library ANN [26].

II. ILLUSTRATION ON TEST CASES

In this section we apply the simulation method to two test cases of analytical distributions of magnetization: transverse uniform magnetization and orthoradial curling (Figure 4). These distributions are chosen to illustrate the method, and understand special features of contrast which can arise in shadow XMCD-PEEM. Although the configurations in Figure 4 are simple models, they are relevant for the experimentally observed magnetic structures observed in cylindrical wires as we will show in the following sections. These two situations have been described analytically for each point, and we checked that an excellent agreement was found with the numerical grid method. In Figure 4, the simulated wire was suspended above the substrate surface so that the complete shadow

is collected. Although this may happen experimentally in some cases (Figure 5b), in most cases the wire is in contact with the supporting surface so that part of shadow is not visible on the screen.

A. Transverse uniform magnetization

Figure 4a shows $I_{X,\sigma}(\mathbf{r})$ and the resulting dichroic absorption for photons going through a wire uniformly magnetized along its diameter. The two curves illustrate the fact that photons with one of the two polarizations is more absorbed than the other due to magnetic dichroism. The dichroic contrast in the shadow is therefore opposite to that at the front surface of the wire, as it simply reflects the effect in the transmitted photons. The polarization dependent propagation of X-rays through the same type of wire is illustrated in Figure 1a. As the sign of dichroism is opposite considering absorbed and transmitted photons, the dichroism observed in the photoemission signal at the back side of the wire may be reversed compared to the front side for thicker wires. The constant contrast and then its gradual decrease on the back side of the wire is illustrated in Figure 4a. There is a critical diameter above which the contrast reverses: $d_c = \ln(\mu_+/\mu_-)/[(\mu_+ - \mu_-)(\sqrt{1-\sin^2\phi})]$ where ϕ is the incidence angle. Obviously, d_c depends on the X-ray energy via the absorption coefficient $\mu_\pm$. In the case of a wire made of Py, and for a grazing angle of 16 ° that is the case at Elettra, d_c is respectively 70, 140, 20 and 50 nm at the Fe-L3, Fe-L2, Ni-L3 and Ni-L2 edges. Note also that the contrast is expected to be larger at the center of the shadow than at its border, because the length of material probed is larger, and so does the imbalance of outgoing photons. These facts highlight that the contrast does not reflect directly the local direction of magnetization, and stresses the need for simulation. Practical examples will be provided in sec.IV, dedicated to the analysis of contrasts.

B. Orthoradial curling

The case of orthoradial curling of magnetization (see right part of Figure 4b) is directly relevant for one type of domain wall in cylindrical wires: the Bloch point wall [13, 27]. In the bottom part of the wire magnetization is mostly pointing left, while in the top part it is mostly pointing right. This leads to a shadow with opposite contrasts on either side. The center of the shadow has no XMCD contrast, as at all points through the wire diameter the X-ray direction is perpendicular to the magnetization direction. This is a clear signature of orthoradial curling. To the contrary, the dichroic contrast at the surface of the wire is maximum close to its top, where the beam is tangent to its surface. It decays on both sides, with a slight negative value on the front side, and a possible inversion of contrast on the backside depending on the total absorption. Thus, the contrast is largely monopolar as in the case of uniform transverse magnetization, which could for instance naively be expected from a transverse wall with the transverse component aligned with the beam direction. Ascribing the surface contrast to a TW or a BPW may remain ambiguous. This example shows that inspection of the shadow may be crucial to get information about a three-dimensional configuration of magnetization.

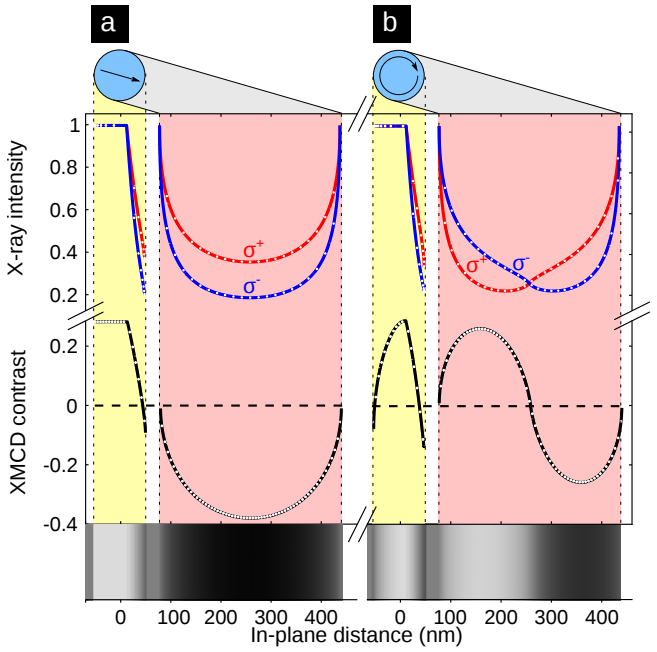

Figure 4: **Illustration of XMCD-PEEM post-processing on two test cases.** The first test case is (a) uniform magnetization across the wire and parallel to the X-ray beam; the second case (b) is orthoradial curling. Photon density and XMCD at the surface of the wire (yellow background) and in the shadow (pink background). The bottom part presents the XMDC contrast for each configuration. The modeled wire is suspended above the surface, so that the entire shadow is visible. Note that the lateral scale is expanded by a factor $\sin(16^\circ) \approx 3.6$ in the shadow, thanks to the grazing incidence

III. COMPARISON WITH EXPERIMENTS

In order to put the above model into practice, we have carried out experiments using XMCD-PEEM on cylindrical wires. In this section, we specify the experimental setup, and discuss the correspondence of the experimentally observed images with those from the simulations.

A. Experimental details

The samples considered are $Fe_{20}Ni_{80}$ (Permalloy) cylindrical wires electroplated in self-organized anodized alumina template. The alumina matrix is dissolved and wires are dispersed on a naturally-oxidized Si supporting surface, aligned along a preferential direction thanks to an in-plane magnetic field applied during dispersion. Their diameter, possibly modulated along the length, ranges from 50 nm to several hundreds of nm. The length of the wires is typically a few micrometers.
Element-selective X-ray absorption spectroscopy (XAS) and XMCD-PEEM were carried out at the spectroscopic photoemission and low-energy electron microscope[28] operated at the undulator beamline Nanospectroscopy of Elettra, Sincrotrone Trieste. The photons impinge on the surface with a grazing angle of 16 °. Spectroscopy was performed across the L edges of either Ni or Fe, using elliptically polarized radiation as a probe. Series of several tens of images with an exposure time of few seconds are recorded, drift-corrected and finally co-added. This yields a high signal-over-noise ratio while limiting drift effects, providing images with a spatial resolution on the order of 30 nm. The level of circular polarization at the Fe and Ni L-edges was estimated to be around 75 % as the X-ray beam is produced by a higher harmonic of the undulator source.

B. Experimental test cases: curling structures

Two types of domain walls may be expected in cylindrical nanowires: of mixed transverse-vortex type for diameter below typically $7\Delta_d$ ($\Delta_d = \sqrt{2A/\mu_0 M_s^2}$), and of Bloch-point type for diameter above typically $7\Delta_d$[27, 29]. The former is reminiscent of domain walls already known in flat strips[30, 31], while the latter is specific to wires with two large dimensions. Consistently, we observed two types of contrast for domain walls in nanowires[13]. Here we illustrate the shadow technique with the Bloch point wall (Figure 5).

Figure 5a shows the XMCD-PEEM image from a magnetic wire of diameter 90 nm, which is suspended above the substrate in the imaged section. The experimental contrast variation is reproduced in the simulation in Figure 5b. Thus, the DW can be unambiguously ascribed to a Bloch point wall. The striking feature is the dual bright and dark contrasts in the shadow, revealing an orthoradial curling as already seen in Figure 4b. The symmetry with respect to a plane perpendicular to the wire axis shows that curling is purely orthoradial, which is compatible only with the Bloch-point wall[27]. The quantitative comparison can be discussed by *e.g.* examining a cross-section (Figure 5d). The contrast has been normalized so that the maxima coincides at the surface of the wire. Compared to simulations, the experimental cross-section is wider by approximately 25 nm on either side, which is consistent with the expected instrumental spatial resolution. The agreement is excellent at the surface of the wire, especially the rather sharp maximum and its location away from the central part of the wire, reflecting the asymmetric shape of the signal (Figure 5d-insert). The XAS should have the shape as shown on the top part of Figure 4. However the instrumental convolution makes it a rather symmetric shape however shifted of the XMCD maximum. In the shadow, the cross-section is clearly antisymmetric, as expected. The cancellation of contrast

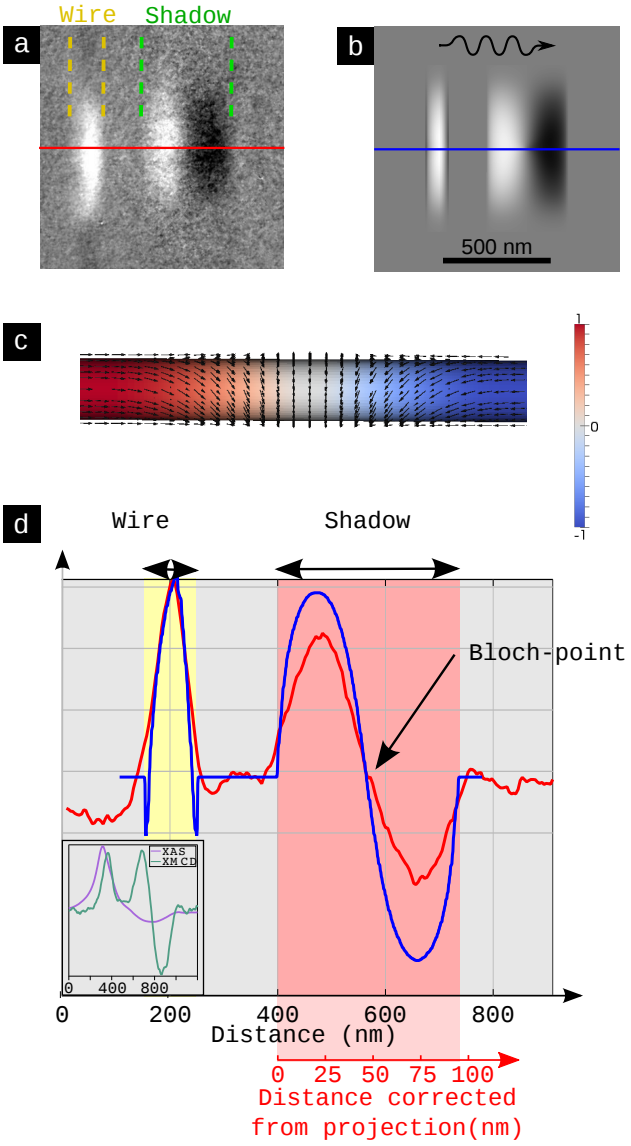

Figure 5: **Comparison of experiment and simulation for the Bloch-Point wall** (a) Experimental and (b) simulated contrasts at the surface and in the shadow (resp. left and right in both images) at the Fe L3 edge for a wire of diameter 90 nm. This diameter has been determined from the XAS of the wire shadow. (c) Micromagnetic simulation of a Bloch-point wall, used as an input for simulating the contrast (d) Cross-sections for (a) and (b). The insert shows the XAS (violet) and XMCD (green) spectra for the experimental contrasts (a).

Table II: The absorption coefficient values used for the simulations in Figure 6.

	(l) Fe L3	(n)
μ_- (nm^{-1})	0.018	0.036
μ_+ (nm^{-1})	0.01	0.02

at the core of the shadow should coincide with the location of the Bloch point. The experimental contrast is however lower than expected in the shadow, which will be discussed in sec.IV. Note also that the lateral scale is expanded by a factor $\sin(16°) \approx 3.6$ in the shadow, thanks to the grazing incidence. The potential of this effect to gain spatial resolution will also be addressed in the next section.

The type and structure of head-to-head domain walls in nanowires is largely determined by the need to lower magnetostatic energy, giving rise to curling along one or more axes[27]. Magnetostatic energy is also present in the vicinity of modulations of diameter along the wire, and at its ends. The occurrence of longitudinal curling structures has been predicted at such locations [32, 33]. Such curling structure have remained elusive experimentally so far. What has been reported are hints for the spread of charges, which however could also be argued to take the form of a 'C' end domain[34, 35]. Shadow PEEM again provides a direct proof for the existence of such structures. Figure 6(e,g-j) show XMCD contrast of a wire at various absorption edges. Figure 6f presents the XMCD contrast arising from a micromagnetic configuration. Thanks to the simulated contrast we can formally identify the contrast at the end as an orthoradial curling structure.

IV. DISCUSSION ON CONTRAST

In this section we discuss in more details several instrumental aspects specific to the shadow imaging geometry, which have an impact on the magnetic contrast or spatial resolution. Of special importance for the shadow imaging of 3D objects are the plane of focus, the start voltage (STV, a voltage bias on the sample which determines the electron kinetic energy), the microscope background level photon energy, the Fresnel diffraction of X-ray from the nonuniform wire shape.

A. Microscope settings

While a rather flat surface may be entirely set close to focus, the case of three-dimensional objects lying on a surface is different. of focus of the instrument is several micrometers, large enough so that the top of the wire and the supporting surface are both in focus. In practice however, this could not be achieved due to the field distortion caused by the wire shape that creates a strong lens effect. For each image, one may thus decide to set the focus anywhere between the top surface of the wire, to the supporting surface. For instance, setting the focus on the supporting surface has a dramatic effect on loosing sharpness and therefore XAS and XMCD contrast on the wire, due to the small lateral size of the wire compared to the shadow projected on the supporting surface the wire being blurred (Figure 7a,b). Blurring effects are decreased upon increasing the start voltage, for reasons described below.

Second, to extract electrons there is a high voltage that is 18 keV− STV. The start voltage (STV) is an additional bias, which is related to the electron kinetic energy (with an additional offset due to work function difference between sample and the LaB6 source used as reference for the energy scale). The non planar wires we use create a nonuniform potential profile of the surface which distorts the imaged electron wave. The lower the electron energy the more pronounced such a distortion. That might explain why the image quality both in the wire and in the shadow is better in Figure 7e than Figure 7d Another effect due to the STV is the change of the inelastic mean free path of importance for emission from the wire surface. If there is a non uniform magnetization along the depth, at low energy, a long mean free path results in a blurred magnetic image.

A fine tuning of the start voltage may also be used to enhance the signal originating from either the wire surface or the shadow. Indeed the materials giving rise to photoemission are different (here permalloy or Si), as well as their capping, so the energy distribution and yield of secondary photoelectrons are different for the part of the image (Figure 7f). In the present case a lower start voltage ($\approx$ 2.0 eV) maximized the number of electrons emitted in the shadow, whereas a higher start voltage ($\approx$ 2.8 eV) resulted in a higher intensity from the wire surface the wire surface Figure 7e. XAS being the measure of emitted electrons, these effects of start voltage are directly transferred to the XAS image. As XMCD is a difference normalized to a sum, its magnitude should not depend on the number of electrons and thus be insensitive to the choice of start voltage. However, as will be argued in sec.IV C, in practice a lower number of emitted electrons reduces the XMCD signal with respect to the computed value, so the start voltage also has an impact on the relative level of contrast on the wire versus the shadow.

B. Photon energy

For 3d ferromagnetic metals the photon energy needs to be tuned close to the maximum of an L3 edge to maximize the contrast. Attention should be paid to the fact that surface oxidation of even a couple of nanometers at the surface of the sample, induces a sub-structure in the L3 peak, and slightly shifts its maximum with re-

spect to a metallic spectra (Figure 1b), while XMCD remains maximum at the location of the peak of metal. Accordingly we found more efficient to use an absorption spectrum taken in the shadow to set the working photon energy, as this probes the bulk of the wire, with no oxidation. In practice, we worked at the Fe L3 edge, which despite the low concentration of Fe proved to yield a larger contrast than the Ni L3 edge both at the surface and in the shadow of the wires. This will be addressed in sec.IV C.

We showed in sec.II that a positive XMCD contrast on the wire should be associated with a negative XMCD contrast in the shadow: a larger absorption and thus loss of photons of a given helicity is associated with an enhanced number of secondary electrons. The number of photons going through the wire depends on the dimensionless quantity $d\mu_{\pm}$, with d the diameter of the wire. The effect of varying this quantity is illustrated by a movie of the wire and its shadow upon ramping the photon energy from below Fe L edges to above Ni L edges (see supplementary materials). For large enough $d\mu_{\pm}$ the imbalance of photons with opposite helicities may be large enough on the backside of the wire so as to outweigh dichroism, so that the contrast on the wire may be reversed from front to back side even for the same direction of magnetization. This expectation is clear on Figure 4, and had been reported experimentally previously[10]. To illustrate the expected impact of $d\mu_{\pm}$ on the front, back and shadow contrast Figure 6(a,c) displays the XMCD contrast of a BPW in the same wire with two different couples of absorption coefficients (Table II). Figure 6b,d presents their profiles. In case of a higher $d\mu_{\pm}$ factor there is a contrast inversion at the back side of the wire (Figure 6c and d). In practice, combining images of the same area varying μ may be useful to refine the analysis. To illustrate this, Figure 6(f-i) show XMCD images of the same wire computed at the $L2$ and $L3$ edges of both Fe and Ni. A large value of μ and of the difference $\mu_+ - \mu_-$ is potentially an advantage for areas where the through-thickness is moderate, to maximize contrast, while a low value of μ is potentially a better choice in the case of long distances traveled through the wire, to keep a reasonable signal-over-noise ratio (see discussion in sec.V B).

C. Background level in PEEM imaging

On a theoretical basis the contrast in the shadow could reach arbitrarily high values for high μd, which however comes at the expense of much reduced intensity. This is the principle of some polarizers, for example for the helicity of X-rays [36] or spin of electrons [37]. Aside from obvious issues arising from the signal over noise ratio, we found out that in practice an instrumental effect limits the contrast. Figure 8 shows the level of XAS collected electrons across a broad wire and its shadow. For this broad wire $\mu_{\pm} d \gg 1$, so that the intensity in the shadow should be vanishingly small. To the contrary, although the intensity reaches a plateau inside the shadow, it remains close to 7 % of the intensity over the free supporting surface. This intensity is not related to the background electronic level of the camera, which is already subtracted from the images. Instead, it reflects electrons that truly impinge on the detector. The physical origin of this background is not straightforward, as it was found to be only weakly affected by changing settings of the LEEM, in particular aperture for the field of view, rejecting electrons from the imaging column electrons outside the field of view, to avoid their incoherent contribution to the image. The contrast aperture, affecting the angular collection of the microscope, does not have a sizeable impact either. At any rate, an (a priori) helicity-independent background intensity reduces the computed XMCD as its difference in the numerator is zero, while its sum in denominator is non-zero. If the background intensity $I_{e,\mathrm{b}}$ is known, then a more accurate view of the true XMCD is achieved by computing: $I_{\mathrm{XMCD},0} = (I_{e,\sigma_-} - I_{e,\sigma_+})/(I_{e,\sigma_-} + I_{e,\sigma_+} - 2I_{e,\mathrm{b}})$. In these it is striking that the contrast in the shadow is enhanced, as expected from theory. This has been done in Figure 6(k-n). These contrasts also illustrate that working at the Fe edges yields a higher contrast than at the Ni edges, whereas a similar contrast would be expected for Permalloy as computed from the tabulated absorption coefficients (Table I), and is explained simply by the existence of the background level.

D. Scattering effects

In general interaction of X-rays with matter can be described via the complex atomic scattering factors. The real and imaginary parts give rise to the Faraday rotation of the photon polarization vector and to magnetic dichroism, respectively, as the photon beam propagates through the magnetic material. The two are related by the Kramers-Kronig transformation, and they are comparable in magnitude at the Fe L3 edge [38].

Until now, we have considered only the x-ray absorption coefficient, which is proportional to the imaginary part of the forward scattering amplitude via the optical theorem [39]. Instead, as we noted above, a proper treatment should include the full scattering process. Indeed, intensity oscillations near the shadow edge are visible in Figure 8 due to Fresnel diffraction from the wire. Furthermore, the Fresnel fringes also show a dichroic signal. The sign of this dichroic signal is opposite to that observed within the shadow, as expected from the inverted absorption signal in transmission.

Nevertheless, the shadow (or the substrate) is in the very near field of the wire, and coherent scattering effects are limited to the shadow edge. The Fraunhofer region at this wavelength (about 1.8 nm) and for a wire diameter below 100 nm does not start until after tens of microns. Therefore, our analysis relating the dichroism within the shadow to the absorption coefficient is valid except at the

very edge of the shadow.

V. DISCUSSION ON SPATIAL RESOLUTION

In this last section we discuss spatial resolution effects specific to shadow imaging.

A. Electric-field related distortion

First, it is known that LEEM images of non-planar surface are distorted[1]. The physical phenomenon is that secondary electrons escape the material perpendicular to the local surface, on the average. Thus their trajectory is curved through the extraction voltage, the curvature of the object providing the same effect as a lens as shown on Figure 3b. Moreover the complex topography of the sample acts as a cathode for the accelerating voltage. Therefore the accelerating voltage is not uniform across the surface. This creates a significant distortion to the outgoing low-energy electron wave. The LEEM image of convex and topographically complex objects such as the wires considered here, is therefore expected to display a larger size than the real object. Obviously this phenomenon is absent in the shadow, as the trajectory of photons is only weakly affected by the circular shape of the wires, due to the optical index being very close to unity. For wires lying perfectly on the supporting surface this effect cannot be checked, because the direct and shadow contrasts overlap. In a few cases a gap was found between wires and surface, large enough to separate the direct and shadow areas (Figure 5b). On these the apparent width of the wire deduced from XAS images indeed was about 50 % larger on the wire than in the shadow. To minimize systematic errors, the figures for wire diameter mentioned in the manuscript and used for simulations, have always been those deduced from the shadow and deconvoluted from the expected 30 nm experimental resolution.

B. Signal over-noise ratio in the shadow

Not only is the shadow more faithful as just discussed, but it may promise for an increase of spatial resolution by a factor $\sin(16°) \approx 3.6$ thanks to the projection with a rather grazing incidence. This would bring the spatial resolution along one direction below 10 nm. A practical limitation for this gain is the lower number of electrons collected in the shadow, degrading the signal-over-noise ratio as estimated below. Let N be the number of electrons emitted from the supporting surface under direct illumination, per given time and area. N_b and N_sh are similarly the number of electrons contributing to the background level, and those contributing to the shadow and related to photons transmitted through the wire, again per unit area and time. In our case $N_\mathrm{b}/N \approx 0.07$ and $N_\mathrm{sh}/N \approx \exp(-\mu d)$, with d the diameter of the wire. The shortest spatial variation that can be expected on the detector is the instrumental resolution σ_instr, resulting in a slope $f' = tN_\mathrm{sh}/\sigma_\mathrm{instr}$ with t the averaging time. When analyzing experimental data, the possible error on lateral resolution σ_x resulting from the vertical error bar σ_y is such that $\sigma_y/\sigma_x = f'$ (see Figure 9). We thus have: $\sigma_x = \sigma_\mathrm{instr}(\sigma_y/tN_\mathrm{sh})$. Taking into that $\sigma_y = \sqrt{tN_\mathrm{b}} + \sqrt{tN_\mathrm{sh}}$, one finally gets:

$$\sigma_x = \frac{\sigma_\mathrm{instr}}{\sqrt{tN_\mathrm{sh}}}\left(1 + \sqrt{\frac{N_\mathrm{b}}{N_\mathrm{sh}}}\right) \tag{3}$$

In the absence of background level Eq. (3) boils down to the usual statistics: $\sigma_x = \sigma_\mathrm{instr}/\sqrt{tN_\mathrm{sh}}$. Thus in theory an image of quality similar to that outside the shadow with integration time t_0, could be obtained at the expense of an increase in integration time up to t_sh such that $\sqrt{t_\mathrm{sh}N_\mathrm{sh}} = \sqrt{t_0 N}$, so with an increase $N/N_\mathrm{sh} = \exp(\mu d)$. This ratio is of the order of $10^2 - 10^4$ for a wire with a diameter of 100 nm at the Fe-$L3$ edge. However in the case of non-zero background level, fluctuations in N_b contribute to the increase of σ_y and thus of σ_x. If N_sh becomes small compared to N_b, based on Eq. (3) the time required to get an image of similar quality is $t_\mathrm{sh} = t_0(N/N_\mathrm{sh})^2(N_\mathrm{b}/N)$, thus with now the power law $\exp(2\mu d)$. For a diameter 100 nm, the power law is now proportional to $10^4 - 10^8$ at the Fe $L3$ edge which becomes prohibitively large. It is the same effect of limited statistics, which limits the signal-over-noise ratio of dichroism in the shadow. While in sec.IV B we saw that dichroism should asymptotically reach 100% in deep shadows ($\mu d \gg 1$), one can show that in practice the signal-over-noise is maximum for $\mu d \approx 1$.

VI. DISCUSSION AND CONCLUSION

At this stage a comparison may be made with the transmission X-ray microscope (TXM). Indeed both TXM and shadow-PEEM allow for probing the volume magnetization integrated along the photon beam. An advantage of TXM is its all-photon basis, making it easily compatible with applied magnetic fields. Also, the sample may be rotated to some extent, gaining information on different directions of magnetization or integration. On the reverse, shadow-PEEM provides the combination of surface and volume information, which may be crucial to solve complex three dimensional magnetization distributions. The potential increase of spatial resolution is also unique. Experiments may even be designed with magnetic objects tilted on purpose to a chosen angle to make the best use of this gain.

To conclude, we have discussed quantitatively physical and instrumental features specific to shadow-PEEM imaging of three-dimensional objects lying on a supporting surface. We have considered in more detail XMCD

imaging and simulation of the expected contrast from micromagnetic simulations. This technique uniquely provides the combination of surface and volume sensitivity in the signal measurement, with an enhanced XMCD contrast and several-fold gain in spatial resolution along the beam direction for the latter. Several effects mentioned need however to be considered to extract true spatial and contrast information such as plane of focus, extraction voltage, electric field distortion and background level.

Acknowledgements

We thank A. Sala (ELETTRA) for assistance in the XMCD-PEEM measurements, J. Vogel, J. -M Tonnerre and S. Pizzini (Institut NEEL), and R. Belkhou (Synchrotron Soleil) for useful discussions. The research leading to these results has received funding from the European Community's Seventh Framework Programme (FP7/2007-2013) under grant agreements n°312284 and 309589..

[1] C. M. Schneider and G. Schönhense, Rep. Prog. Phys. **65**, R1785 (2002).
[2] P. Fischer, T. Eimüller, G. Schütz, G. Denbeaux, A. Pearson, L. Johnson, D. Attwood, S. Tsunashima, M. Kumazawa, N. Takagi, et al., Rev. Sci. Instr. **72**, 2322 (2001).
[3] T. Kasama, R. E. Dunin-Borkowski, and M. Beleggia, Holography - Different Fields of Application (Intech, 2011), review, magnetism, instrumentation Chapter 3: Electron Holography of Magnetic Materials, URL http://www.intechopen.com/books/holography-different-fields-of-application/electron-holography-of-magnetic-materials.
[4] J. Zweck and T. Uhlig, Novel techniques for characterizing and preparing samples (Wiley, 2007), vol. 3 of Hanbook of Magnetism and advanced magnetic materials, experiment, instrumentation, review Lorentz microscopy of thin-film systems, pp. 1393–1427.
[5] J. N. Chapman and M. R. Scheinfein, J. Magn. Magn. Mater. **200**, 729 (1999).
[6] R. Allenspach, IBM J. Res. Develop. **44**, 553 (2000).
[7] N. Rougemaille and A. K. Schmid, Europhys. J.: Appl. Phys. **50**, 20101 (2010).
[8] E. Bauer, Rep. Prog. Phys. **57**, 895 (1994).
[9] J. Kimling, F. Kronast, S. Martens, T. Böhnert, M. Martens, J. Herrero-Albillos, L. Tati-Bismaths, U. Merkt, K. Nielsch, and G. Meier, Phys. Rev. B **84**, 174406 (2011).
[10] R. Streubel, V. P. Kravchuk, D. D. Sheka, D. Makarov, F. Kronast, O. G. Schmidt, and Y. Gaididei, Appl. Phys. Lett. **101**, 132419 (2012), ISSN 0003-6951, URL http://dx.doi.org/10.1063/1.4756708.
[11] O. Sandig, J. Herrero-Albillos, F. Römer, N. Friedenberger, J. Kurde, T. Noll, M. Farle, and F. Kronast, J. Electron Spectr. Rel. Phenom. **185**, 365 (2012), ISSN 0368-2048, URL http://dx.doi.org/10.1016/j.elspec.2012.07.005.
[12] J. Zabaleta, S. Valencia, F. Kronast, C. Moreno, P. Abellan, J. Gazquez, H. Sepehri-Amin, F. Sandiumenge, T. Puig, N. Mestres, et al., Nanoscale **5**, 2990 (2013), ISSN 2040-3372, URL http://dx.doi.org/10.1039/c3nr33346a.
[13] S. Da Col, S. Jamet, N. Rougemaille, A. Locatelli, T. O. Mentes, B. S. Burgos, R. Afid, M. Darques, L. Cagnon, J. C. Toussaint, et al., Phys. Rev. B **89**, 180405 (2014), URL http://link.aps.org/doi/10.1103/PhysRevB.89.180405.
[14] E. Snoeck, C. Gatel, L. M. Lacroix, T. Blon, S. Lachaize, J. Carrey, M. Respaud, and B. Chaudret, Nano Lett. **8**, 4293 (2008).
[15] F. Cheynis, A. Masseboeuf, O. Fruchart, N. Rougemaille, J. C. Toussaint, R. Belkhou, P. Bayle-Guillemaud, and A. Marty, Phys. Rev. Lett. **102**, 107201 (2009).
[16] O. Fruchart, N. Rougemaille, J. C. Toussaint, R. Belkhou, Y. Tian, H. Yu, F. Cheynis, A. Masseboeuf, P. Bayle-Guillemaud, and A. Marty, IEEE Trans. Magn. **46**, 1552 (2010).
[17] A. Fernandez-Pacheco, L. Serrano-Ramon, J. M. Michalik, M. R. Ibarra, J. M. De Teresa, L. O'Brien, D. Petit, J. Lee, and R. P. Cowburn, Sci. Rep. **3**, 1 (2013), URL http://dx.doi.org/10.1038/srep01492.
[18] N. Biziere, C. Gatel, R. Lassalle-Balier, M. C. Clochard, J. E. Wegrowe, and E. Snoeck, Nano Lett. **13**, 2053 (2013).
[19] R. Streubel, J. Lee, D. Makarov, M.-Y. Im, D. Karnaushenko, L. Han, R. Schäfer, P. Fischer, S.-K. Kim, and O. G. Schmidt, Adv. Mater. **26**, 316 (2014).
[20] V. D. NĠuyen, S. Pizzini, J. Vogel, O. Fruchart, J. C. Toussaint, and N. Rougemaille, unpublished.
[21] R. Nakajima, J. Stöhr, and Y. U. Idzerda, Phys. Rev. B **59**, 6421 (1999).
[22] T. O. Mentes and A. Locatelli, J. Electron Spectr. Rel. Phenom. **185**, 323 (2012), ISSN 0368-2048, URL http://dx.doi.org/10.1016/j.elspec.2012.07.007.
[23] F. Alouges, E. Kritsikis, and J.-C. Toussaint, Physica B **407**, 1345 (2012).
[24] H. S. M. Coxeter, Introduction to Geometry, 2nd ed. (Wiley, 1969), p. 218.
[25] http://doc.cgal.org/4.5.2/manual/packages.html.
[26] http://www.cs.umd.edu/ mount/ann/.
[27] S. Jamet, Rougemaille, J. C. Toussaint, and O. Fruchart, Magnetic Nano- and Microwires: Design, synthesis, properties and applications (Woodhead Publishing, in press).
[28] A. Locatelli, L. Aballe, T. O. Menteş, M. Kiskinova, and E. Bauer, Surf. Interf. Analysis **38**, 12 (2006).
[29] A. Thiaville and Y. Nakatani, Spin dynamics in confined magnetic structures III

(Springer, Berlin, 2006), vol. 101 of Topics Appl. Physics, theory, simulation, magnetism, review Domain-wall dynamics in nanowires and nanostrips, pp. 161–206.

[30] R. McMichael and M. Donahue, IEEE Trans. Magn. **33**, 4167 (1997).

[31] Y. Nakatani, A. Thiaville, and J. Miltat, J. Magn. Magn. Mater. **290-291**, 750 (2005).

[32] P. Landeros, O. J. Suarez, A. Cuchillo, and P. Vargas, Phys. Rev. B **79**, 024404 (2009).

[33] S. Allende, D. Altbir, and K. Nielsch, Phys. Rev. B **80**, 174402 (2009).

[34] T. Wang, Y. Wang, Y. Fu, T. Hasegawa, H. Oshima, K. Itoh, K. Nishio, H. Masuda, F. S. Li, H. Saito, et al., Nanotechnology **19**, 455703 (2008).

[35] S. Vock, C. Hengst, M. Wolf, K. Tschulik, M. Uhlemann, Z. Sasvari, D. Makarov, O. G. Schmidt, L. Schultz, and V. Neu, Appl. Phys. Lett. **105**, 172409 (2014), ISSN 1077-3118, URL http://dx.doi.org/10.1063/1.4900998.

[36] J. B. Kortright, S.-K. Kim, T. Warwick, and N. V. Smith, Appl. Phys. Lett. **71**, 1446 (1997).

[37] D. P. Pappas, K.-P. Kämper, B. P. Miller, and H. Hopster, Phys. Rev. Lett. **66**, 504 (1991).

[38] J. B. Kortright and S. K. Kim, Phys. Rev. B **62**, 12216 (2000).

[39] J. D. Jackson, Classical Electrodynamics (1975).

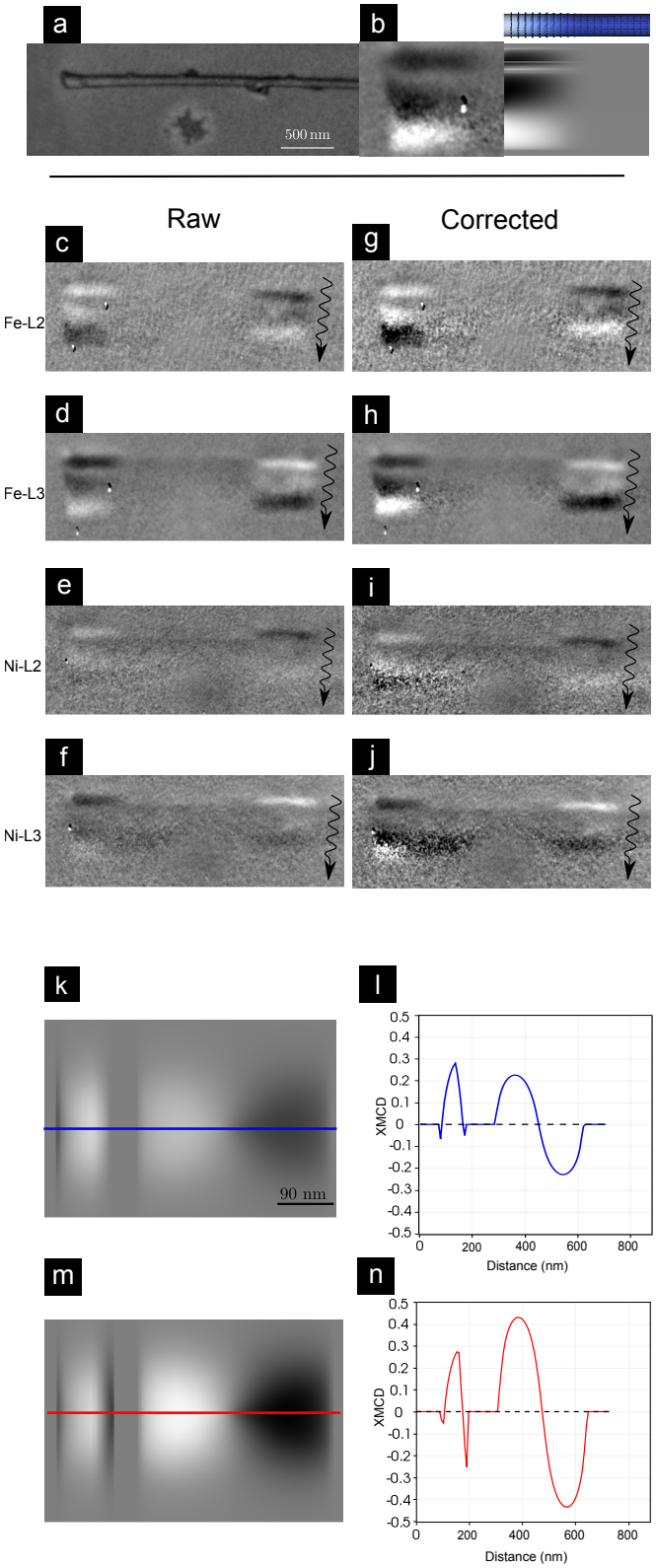

Figure 6: **Role of the absorption coefficient on the contrast.** (a) LEEM image of a wire and (c)-(f) experimental XMCD contrasts of this wire. (g)-(j) are the same experimental contrasts from which the background level has been removed. (b) left is the left end of (h) and to the right is a simulation of the XMCD contrast at the Fe L3 edge for a wire of 120 nm diameter with a curling at the end and the corresponding micromagnetic configuration. Simulated XPEEM images for a 90 nm-diameter wire with a Bloch point wall (see absorption coefficients Table II) and their profiles (l) and (n). For (c,d,g,h) the contrast is 6 %, it is 9 % for (f,j) and 5 % for (e,i).

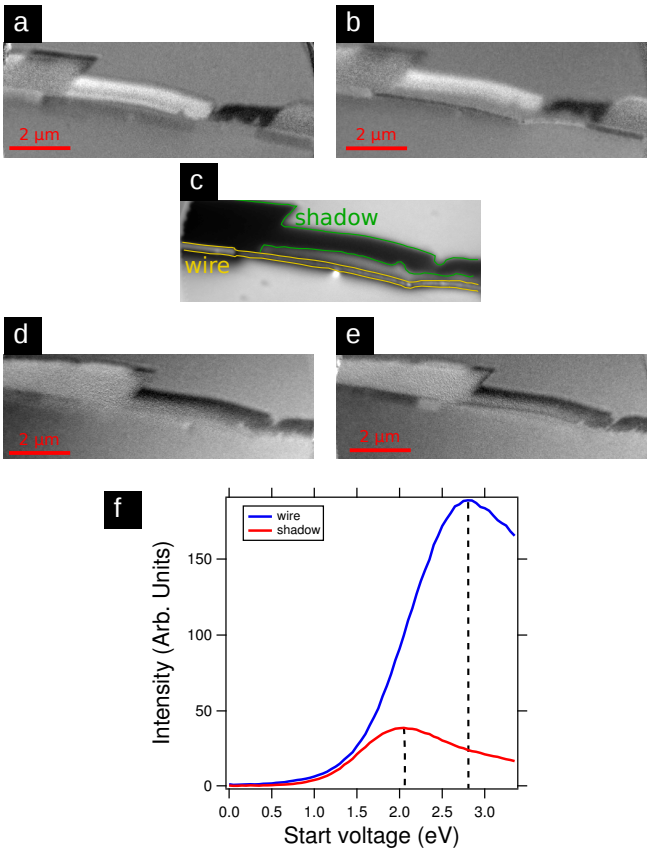

Figure 7: **Role of the plane of focus and the start voltage)** The XMCD contrast is taken at the Fe L3 edge, with start voltage 2.1 eV with a focus (a) on the surface and (b) on the wire. (c) is the sum of both helicity intensities where the wire and shadow areas are highlighted to guide the eye. (d) 2.0 eV and (e) 2.8 eV with a focus on the surface. (f) XAS on the wire and the shadow versus the start voltage.

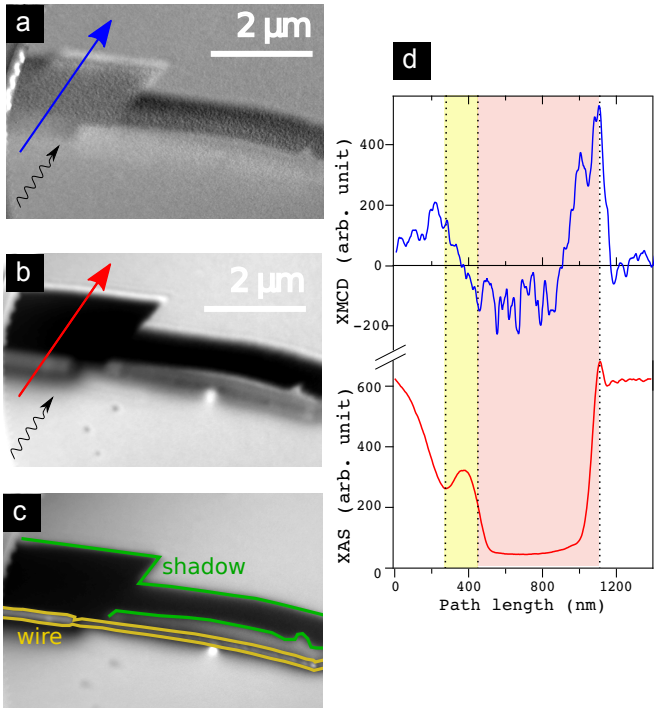

Figure 8: **Scattering effects.** Wire image of the intensity for (a) the XMCD and (b) the absorption contrast summed for both helicities. (c) shows the wire and shadow zones on the contrast images. The plot (d) presents the intensity at the cross-sections shown in (a) and (b). Dotted lines are guides to the eyes and limit wire (left and shadow areas.

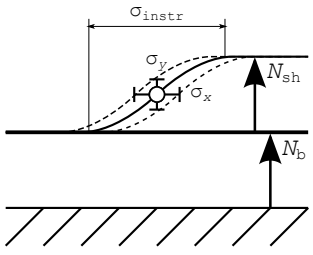

Figure 9: **Signal over noise ratio**